# SHAPE OF THE SPECTRAL LINE AND GAMMA ANGULAR DISTRIBUTION OF THE $^{12}C(p, p'\gamma_{4.44})^{12}C$ REACTION

K. Rusiecka†, A. Wrońska, A. Magiera, G. Gazdowicz
G. Obrzud

M. Smoluchowski Institute of Physics, Jagiellonian University
Kraków, Poland

L. Kelleter, K. Laihem, J. Leidner, A. Stahl

Physics Institute 3B, RWTH Aachen University, Aachen, Germany

A. Chrobak, A. Konefał

Department of Nuclear Physics and Its Applications, Institute of Physics
University of Silesia, Katowice, Poland

*(Received February 14, 2018; accepted July 17, 2018)*

A model explaining the shape of the spectral line in the $^{12}C(p, p'\gamma_{4.44})^{12}C$ nuclear reaction has been applied to data collected during an experiment conducted at the Heidelberg Ion-Beam Therapy Center. Spectra were recorded for a graphite target setup, initial proton beam energies of 70.54 MeV and 88.97 MeV, which were later degraded before reaching the main target, and detection angles ranging from 90° to 150°. The model calculations reproduced experimental data and determined the angular distribution of the nuclear reaction. This article presents the details of the model along with a description of the subsequent analysis steps and results.

DOI:10.5506/APhysPolB.49.1637

## 1. Introduction

The spectral line stemming from the nuclear reaction $^{12}C(p, p'\gamma_{4.44})^{12}C$ is visible in the gamma spectra obtained at the detection angle of 90° as a double peak. The center of the valley between the two peaks corresponds to the energy of 4438 keV. The double peak becomes asymmetric and shifted when

† Corresponding author: katarzyna.rusiecka@doctoral.uj.edu.pl

the detection angle is changed. The explanation of its shape lies in the interplay of the Doppler effect and the selective population of magnetic sublevels of the first excited state of carbon in the inelastic scattering process [1].

This phenomenon has also been observed in the gamma spectra registered from solar flares and molecular clouds, which makes it interesting for the astrophysical community [2–4]. The $^{12}C_{4.44\to gs}$ spectral line can be produced in several processes, *e.g.* inelastic scattering of protons and $\alpha$ particles from $^{12}C$, and proton- and $\alpha$-induced spallation of $^{16}O$. The contribution to the $^{12}C_{4.44\to gs}$ line stemming from these reactions is usually referred to as a narrow component. This spectral line can also be produced in inversed kinematics by accelerated $^{12}C$ and $^{16}O$ bombarding hydrogen and helium nuclei. However, due to the large velocities of the emitted heavy nuclei, the Doppler broadening is large. Therefore, the contribution to the 4.44 MeV line deriving from these processes is referred to as a broad component [5].

The implementation of the model presented in this article refers to the narrow component produced purely by fast protons impinging on $^{12}C$ nuclei. In this case, the interaction between target nuclei and the incident protons occurs in two stages. The laboratory frame is defined as the frame in which the $^{12}C$ nuclei are initially at rest. In the first step of the reaction, the incident proton causes excitation of the target nucleus. In the second step, deexcitation of the excited nucleus occurs along with the emission of a gamma quantum. Due to the short lifetime of this state, the emission takes place when the excited carbon nucleus is still in motion, thus a Doppler shift occurs. The angular distribution of this process in the rest frame of the excited carbon nucleus is given by [1, 6]

$$W_2\left(\theta_\gamma^{\mathrm{CM}}\right) = \sum_{m=-2}^{m=2} a_m F_2^m\left(\theta_\gamma^{\mathrm{CM}}\right) , \tag{1}$$

where the functions $F_2^m(\theta_\gamma^{\mathrm{CM}})$ are

$$\begin{aligned} F_2^m\left(\theta_\gamma^{\mathrm{CM}}\right) \;=\; & \frac{1}{2}\left[1-\frac{m\,(m+1)}{6}\right]\left|Y_2^{m+1}\left(\theta_\gamma^{\mathrm{CM}},\phi_\gamma^{\mathrm{CM}}\right)\right|^2 \\ & +\frac{1}{2}\left[1-\frac{m\,(m-1)}{6}\right]\left|Y_2^{m-1}\left(\theta_\gamma^{\mathrm{CM}},\phi_\gamma^{\mathrm{CM}}\right)\right|^2 \\ & +\frac{m^2}{6}\left|Y_2^{m}\left(\theta_\gamma^{\mathrm{CM}},\phi_\gamma^{\mathrm{CM}}\right)\right|^2 . \end{aligned} \tag{2}$$

In Eq. (1), $a_m$ is the population of the $m$ magnetic sublevel of the first excited state of the carbon nucleus. The $Y_L^m$ are spherical harmonics, where the choice of the order of $L = 2$ is given by the spin difference between the excited and ground states. The $\theta_\gamma^{\mathrm{CM}}$ stands for the polar angle of the

emission of the gamma quantum, while $\phi_\gamma^{\mathrm{CM}}$ is the azimuthal angle of the emission. The coefficients $a_m$ are *a priori* unknown but can be calculated based on the experimental data for the $^{12}\mathrm{C}_{4.44\to\mathrm{gs}}$ spectral line. However, due to holding the constraints

$$\begin{aligned} \sum_m a_m &= 1\,, \\ a_m &= a_{-m}\,, \end{aligned} \tag{3}$$

it is sufficient to determine only two of them (*e.g.* $a_0$ and $a_2$) to fully describe the shape of the carbon line and the angular dependence of the $^{12}\mathrm{C}_{4.44\to\mathrm{gs}}$ transition. The presence of spherical harmonics in Eq. (1) links the parameters $a_m$ with the shape of the spectral line and the angular distribution of the process.

It needs to be stated that population of magnetic sublevels of the excited target nucleus, in general, depends on the projectile scattering angle in the inelastic scattering reactions. In the conducted experiment, the scattered protons were not detected, though. Therefore, in the presented implementation of the model, the coefficients $a_m$ are averaged over proton scattering angles.

It has been proven by Kolata *et al.* [1] that the kinematic effect itself, in the absence of the selective population of the magnetic sublevels, could not produce the double-peak structure of the carbon line. It is also worth noticing that the details of this structure can be observed when the Doppler shift is larger than the resolution of the detector, *i.e.* the recoil nucleus must be given a sufficiently large energy and the lifetime of the state must be much shorter than the stopping time in the target material.

The significance of the $^{12}\mathrm{C}_{4.44\to\mathrm{gs}}$ line shape model lies in the fact that, theoretically, it allows for the reconstruction of the gamma angular distribution of the nuclear reaction based on a single measurement of the gamma spectrum at one angle, provided that the corresponding angular distribution of inelastic scattering of protons from $^{12}\mathrm{C}$ is known.

The objective of this work was to implement a model describing the shape of the carbon line coming from deexcitation of the first excited state of the carbon nucleus. The model implementation uses Monte-Carlo-based calculations. The required input includes energy distributions of protons interacting with the target nuclei and angular distributions for the first stage of the nuclear reaction *i.e.* $^{12}\mathrm{C}(p,p')^{12}\mathrm{C}^*$. Additionally, information about the angular distribution of the second stage of the reaction is required (Eq. (1)). Then it is possible to construct the angular distribution of the outgoing gamma quanta in the laboratory frame and recreate the shape of the spectral line for specific angles. In the model, this information is compared with the experimental data in order to find the values of the $a_m$ parameters for

which the best agreement is achieved. The method has been described already in [7]. Since that time, the model has been improved by accounting for previously neglected experimental effects. Moreover, in the following, we present a comparison to a different set of experimental data of better quality.

## 2. Experiment

### *2.1. Experimental setup*

The experiment was conducted at the Heidelberg Ion-Beam Therapy Center (HIT) using a proton beam accelerated by the synchrotron to energies ranging from 70.54 to 130.87 MeV.

After leaving the nozzle, the beam was impinging on the phantom consisting of two parts, as shown in Fig. 1. The first part was located at 37 cm downstream from the beam nozzle. It consisted of two wedge-shaped blocks, one of which was moved along the other fixed wedge. Consequently, the amount of the material in the beam path was changing. This part of the target setup served as an energy degrader for the protons. Following the degrader, a thin target of dimensions 5 cm × 5 cm × 1 mm was placed in the beam path at a distance of 59.5 cm from the nozzle. Both, the degrader and the thin target were made of graphite. Such a construction of the phantom allows for the measurement of the angular distribution of gamma radiation originating in the thin target.

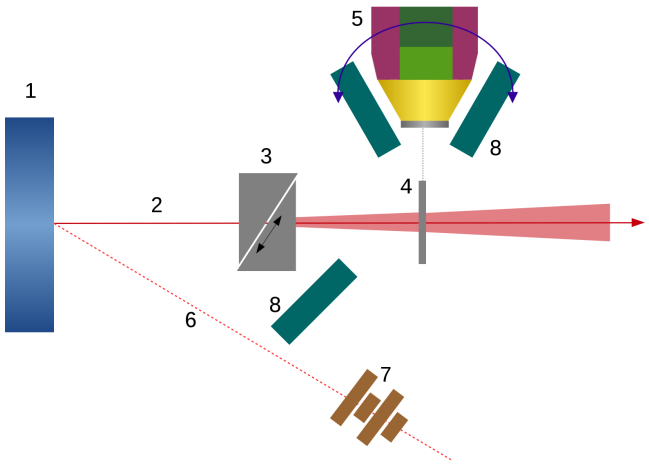


Fig. 1. Scheme of the experimental setup: (1) beam nozzle, (2) beam trajectory, (3) degrader (arrow indicates direction of movement), (4) thin target, (5) HPGe detector with an active Compton shield, (6) trajectory of protons scattered in the nozzle, (7) beam current monitor and (8) lead shielding. Reproduced from [8].

Gamma spectra were recorded from the thin target with the use of a HPGe detector with an active Compton shield. The detector was placed on a movable platform, which allowed for remote control of its angular position. The thin target was the center of rotation. Additionally, a passive shield in the form of a lead sarcophagus for the detector was provided.

A Beam Current Monitor (BCM) made of a telescope consisting of 4 plastic scintillators was placed close to the beam nozzle. The BCM detector was used to register protons scattered from the exit window of the nozzle and thus allowed for relative beam intensity monitoring independently from the thickness of the degrader. The registered number of scattered protons along with the calibration measurements from the EtherCAT system enabled the absolute normalization of the measured spectra.

It needs to be stressed that the experimental conditions were designed to imitate the course of proton therapy and the primary aim of the measurements was to deliver data for future applications in prompt gamma imaging in hadron therapy. However, the excellent spectroscopic quality of the data allowed for the additional analysis of the shape of the $^{12}C_{4.44\to gs}$ spectral line.

### *2.2. Collected data*

All the measurements were divided into series, meaning registration of a set of gamma spectra in the same experimental conditions, but with different settings of the degrader thickness or the angular position of the detector. In the context of the $^{12}C_{4.44\to gs}$ line shape model, the series with a variable angular position of the detector are the most interesting. Two such series have been chosen from all the measurements and they are summarized in Table I.

A more detailed description of the experiment along with a discussion of the results significant for the prompt gamma imaging in hadron therapy may be found in [8].

TABLE I

Details of two experimental series included in the analysis of the carbon line shape.

| | Series A | Series B |
|---|---|---|
| Beam energy | 88.97 MeV | 70.54 MeV |
| Degrader thickness | 35.82 mm | 23.00 mm |
| Mean energy of the protons in the slice | 17.59 MeV | 14.72 MeV |
| Detection angles | 90°, 115°, 130°, 150° | 90°, 120° |

## 3. Data processing

There are two main stages in the data analysis process. In the first stage, the input information is prepared and in the second stage, the model calculation and the analysis of the $^{12}C_{4.44\rightarrow gs}$ line shape is conducted. The most important aspects of the data processing algorithm are described further in this section. The software used for the data analysis and the model calculations has been written with the use of a ROOT framework [9].

### *3.1. The background subtraction*

Experimental gamma spectra are the primary input for the $^{12}C_{4.44\rightarrow gs}$ spectral line shape analysis. In the recorded spectra (see Fig. 2), it is seen that near the spectral line two types of background can be distinguished: a constant continuum visible on the right-hand side of the carbon peak and a Compton continuum on the left-hand side of the peak. The latter can influence the shape of the peak structure and thus a careful background subtraction is necessary.

In order to describe the background accurately, both contributions were modeled separately by a linear fit to the right and a 3$^{rd}$ order polynomial on the left, both outside of the peak region. Subsequently, the contributions were extrapolated to the peak region and joined at the point where they become equal to produce a background model, which was then subtracted from the data. The uncertainties of the data points were increased to include additional contributions from the fit covariance matrix. A comparison of experimental and background-subtracted spectra along with the fitted background functions are presented in Fig. 2.

### *3.2. Energy distribution and angular distribution of protons*

Apart from the experimental spectra, information about the energy of protons interacting with the target nuclei is required in order to carry out model calculations. As mentioned previously, the analyzed data concern the nuclear reactions occurring in the thin target. However, before the proton beam reaches the thin slice, it traverses a certain amount of material (energy degrader). This experimental approach turned out to be very efficient for the prompt gamma radiation measurements. However, it caused an energy straggling of the protons for large degrader thicknesses. Consequently, protons interacting with target nuclei in the thin target were characterized by a continuous energy distribution, which was retrieved from Geant4 simulations [10] (see Fig. 3).

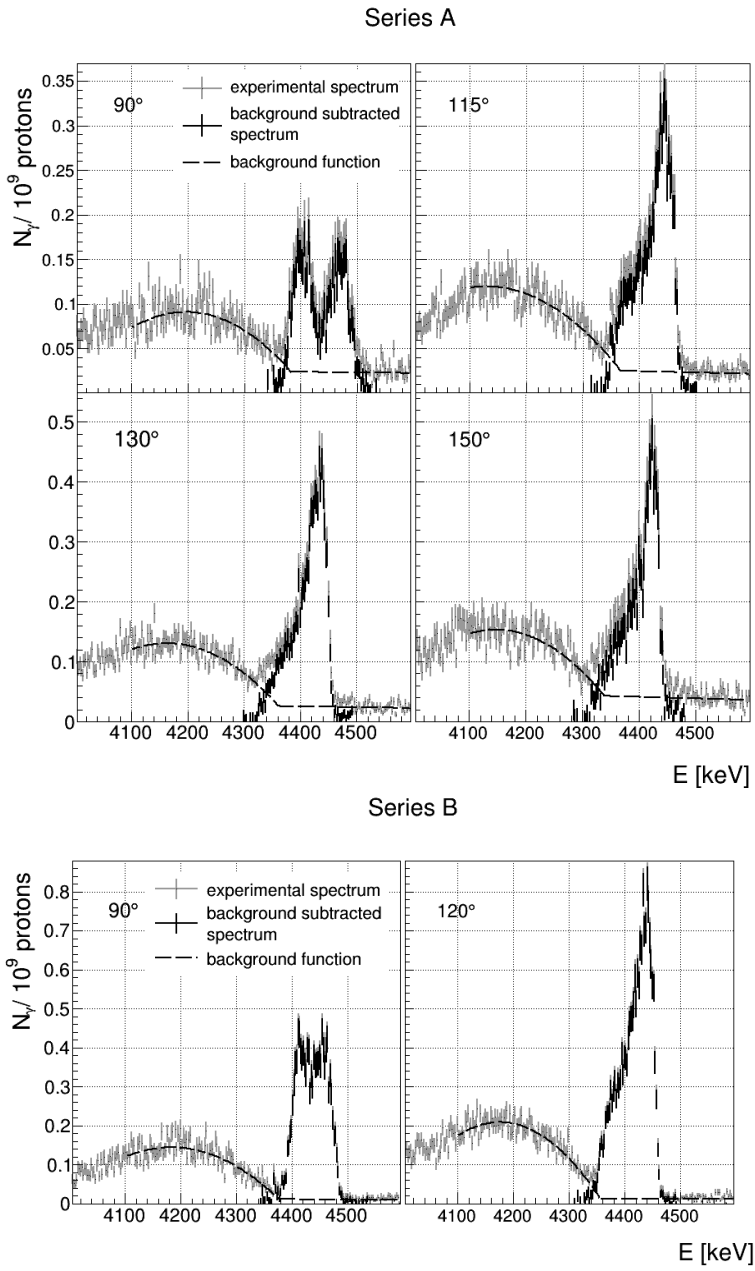


Fig. 2. Experimental carbon lines as measured and after background subtraction. The experimental data has been plotted in gray, the background subtracted spectrum has been plotted in black, and a dashed line is the fitted background function.

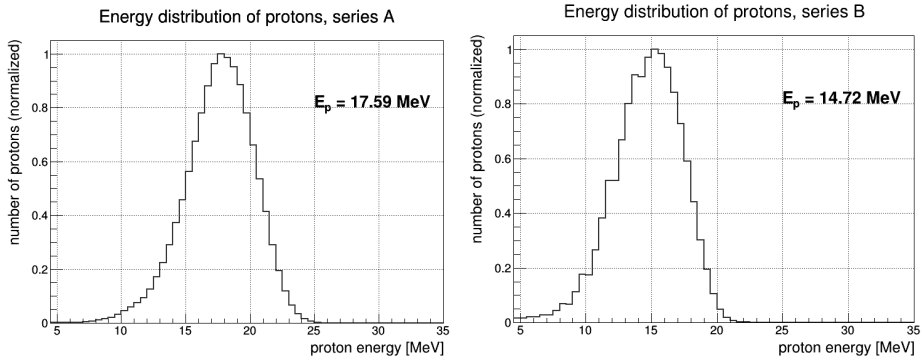


Fig. 3. Energy distributions of protons in the thin slice obtained in the Geant4 simulations. For each histogram, a cut at the energy of 4.81 MeV has been made, since this is the threshold for the nuclear reaction. $E_p$ is the mean proton energy.

Further required input data is the angular distribution of the first stage of the nuclear reaction, *i.e.* inelastic scattering of protons from $^{12}$C. In [7], this information was provided with the use of the Talys package [11]. In order to confirm the validity of Talys calculations, comparative studies of the calculated and experimentally measured angular distributions were conducted. For that reason, a database of experimental data was built. It consisted of angular distributions for 29 energies of incident protons within the energy range from 9.5 MeV to 65 MeV [12–23].

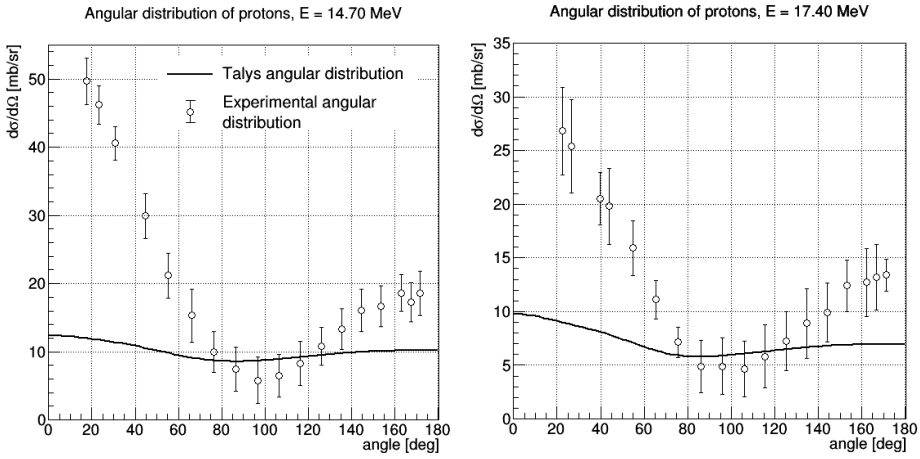


Fig. 4. Comparison of angular distributions of protons generated by Talys (solid line) and experimental data from [22] (circles). The energies of protons chosen for this comparison are the closest ones to the mean energies of protons in the thin slice (see Fig. 3) for which data in the collected base is available.

A detailed comparison of the angular distributions provided by Talys and the experimental data revealed significant differences, an example of which is presented in Fig. 4. The corresponding angular distributions are not consistent in terms of magnitude as well as shapes. Therefore, in the further analysis, the angular distributions calculated by Talys were replaced by the input based on the collected experimental data. The angular distributions for the proton energies which are not available in the database are generated via a bilinear interpolation based on the four nearest points (algorithm provided within the ROOT framework). To cover the ranges of angles where the experimental data is not available (small and large angles), a linear extrapolation was carried out.

### *3.3. Analysis of the shape of* $^{12}C_{4.44\to gs}$ *spectral line*

In order to analyze the shape of the $^{12}C_{4.44\to gs}$ spectral line, a fitting algorithm based on ROOT's MINUIT was developed. The following parameters describing the shape of the studied line were fitted: $a_0$, $a_2$ (coefficients from Eq. (1)) and $h$ (the scaling factor). As stated before, parameters $a_m$ fix the shape of the angular distribution for the $^{12}C(p,p'\gamma_{4.44})^{12}C$ nuclear reaction. Thus, their values are dependent on the energy of the impinging protons rather than the detection angle. For that reason, the fitting procedure included all data from the given experimental series.

$\chi^2$ from all pairs of experimental and theoretical spectra within a single series was calculated according to the formula

$$\chi^2 = \frac{1}{\mathrm{NDF}}\, t \sum_n \frac{(x_n - h\, y_n)^2}{\sigma_{x_n}^2 + h^2\, t\sigma_{y_n}^2}\,, \tag{4}$$

where the summation runs over all bins in the experimental spectra, $x$ is number of entries in the $n^{\mathrm{th}}$ bin of the experimental spectrum, $y$ is corresponding value in the generated theoretical histogram, $\sigma_{\mathrm{E}}$ and $\sigma_{\mathrm{T}}$ are respective uncertainties of those, and NDF stands for the number of degrees of freedom.

Calculation of the theoretical carbon line shape was based on the Monte Carlo method. For each measurement condition, a sample of events for the two-stage reaction was generated uniformly in the respective phase spaces. The cross section of the inelastic scattering of protons from $^{12}C$ was calculated as described in Section 3.2. Additionally, the cross section of the gamma emission by the excited $^{12}C$ nucleus for the given values of the $a_0$ and $a_2$ parameters was calculated according to Eq. (1). Subsequently, the product of those was used as a weight for each event. Model calculations account for the finite size of the detector, its shape and position, *i.e.* the generated gamma quanta have to fit in the angular acceptance of the detector.

The energy of the generated gamma quanta was smeared with the 2-keV energy resolution of the detector. Additionally, an effect of the variable detection efficiency for different gamma energies was taken into account. Finally, the spatial distribution of protons interacting with the target nuclei in the thin target was implemented. The information about spatial distribution of protons was obtained with the Geant4 simulation.

As mentioned in Section 1, excited carbon nucleus decays while still in motion. The halflife time $t_{1/2}$ of the first excited state of $^{12}$C nucleus is 42.2 fs [5, 24]. This is sufficient for recoiling carbon nucleus to be noticeably slowed down in graphite. Therefore, the model has been implemented in two versions: (1) with carbon nucleus moving at a constant velocity and (2) with the recoiling carbon nucleus slowing down in graphite with the stopping power as taken from SRIM package [25]. In order to investigate an influence of nucleus deceleration, all model calculations have been carried out for both scenarios and, subsequently, compared.

As a result, the values of the $a_0$, $a_2$ and $h$ parameters along with their uncertainties were obtained for each experimental series and, consequently, also the best matching line shapes and the associated angular distribution. In the following section, the results of the model calculations assuming decelerating excited carbon nucleus are presented, along with the description of differences between the two model implementations.

## 4. Results and discussion

Obtained results of model calculations with carbon nucleus slowing down for both analyzed experimental series have been listed in Table II. Based on the obtained values, the theoretical carbon lines for each measurement have been generated with the statistics of $10^5$ events. The comparison of the experimental spectral line shape and the corresponding theoretical one are shown in Fig. 5. It can be seen that the shape of the structure is reproduced fairly well, however, some differences are visible. Namely, for the detection angle of 90°, the peaks are slightly overestimated, while for medium detection

TABLE II

Values of parameters describing the shape of the $^{12}C_{4.44\rightarrow gs}$ line.

| Parameter | Series A | Series B |
|---|---|---|
| $a_0$ | $-0.010(70)$ | $0.1675(69)$ |
| $a_2$ | $0.51(12)$ | $0.337(27)$ |
| $h$ | $2.03(30) \times 10^{-7}$ | $3.25(37) \times 10^{-7}$ |

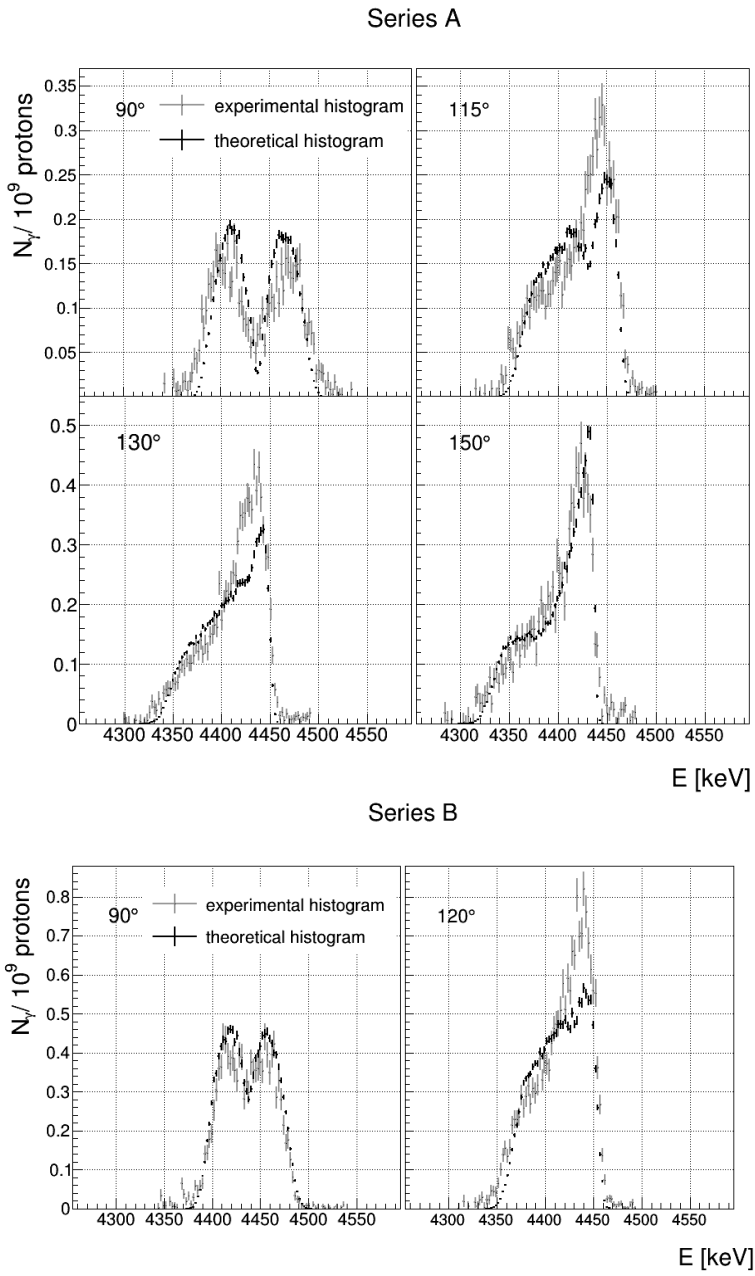


Fig. 5. Comparison of the shape of the experimental carbon line (gray) and the reconstructed carbon line (black). The errors are purely statistical.

angles (115°–130°), the sharp part of the peak is underestimated. The theoretical carbon line for 150° shows the best agreement with the experimental data. The source of those differences may lie in the angular distributions of the inelastic scattering of protons from $^{12}$C. As described in previous sections, the angular distributions for proton energies that were unavailable in the collected database were constructed via interpolation. Additionally, an extrapolation was performed for small and large angles, where experimental data was lacking. This extrapolation can significantly influence further calculations, especially for small angles, where the cross section for inelastic scattering is expected to grow rapidly.

In order to confirm the validity of the fitting algorithm, $\chi^2$ distribution maps were constructed. For the map construction, the $h$ parameter has been fixed, and a theoretical carbon line was generated on a grid of $a_0$ and $a_2$ parameter values. Subsequently, $\chi^2$ was calculated for each set of experimental and theoretical histograms according to Eq. (4). The maps for both experimental series are shown in Fig. 6. In both cases, the distributions have relatively large ellipse-shaped minima, which are inclined to the horizontal axis. This is an indication that parameters $a_0$ and $a_2$ are correlated. In addition, parameters $a_0$ and $a_2$ as determined by the fitting procedure have been marked in both maps with an asterisk. For series A as well as series B, the position of an asterisk lies in the visible minimum of the distribution, which confirms the validity of the fitting results. It can be seen that for series A, the minimum is located close to the edge of the physical region, but on the outer side of it. However, the parameters values are consistent with the corner of the physical region within their uncertainties.

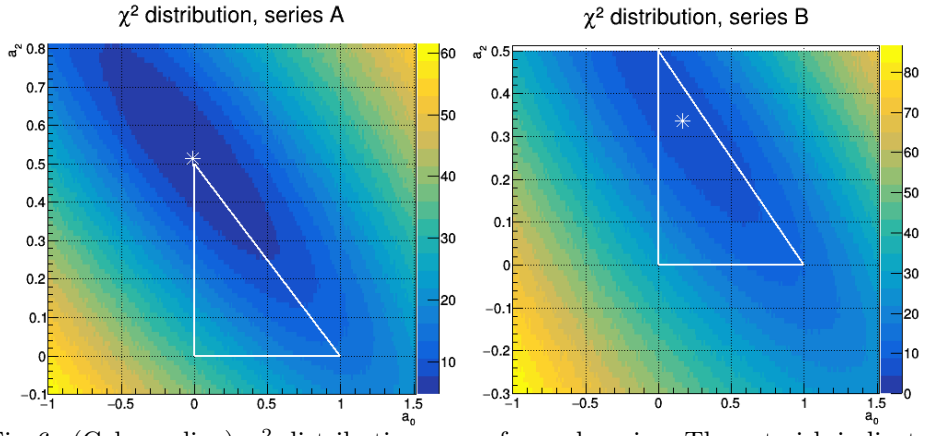


Fig. 6. (Color online) $\chi^2$ distribution maps for each series. The asterisk indicates values of the parameters $a_0$ and $a_2$ determined by the model. The triangle indicates the area where parameters have physically valid values, which is a result of Eq. (3).

Additionally, the results of the fit have been confirmed by multiple tests of the fitting conditions, including modification of the starting parameters and their ranges and using different samples of events during the generation of the theoretical carbon lines. For all tests, the results remained consistent within statistical uncertainties.

The angular distribution for the $^{12}\mathrm{C}(p,p'\gamma_{4.44})^{12}\mathrm{C}$ reaction has also been investigated. The experimental angular distribution for series A has been obtained as integrals of the background-subtracted experimental carbon lines as a function of the detection angle, where additional points symmetric with respect to 90° were added. Similarly, the theoretical angular distribution has been constructed. A sum of Legendre polynomials as follows:

$$W(\theta) = b_0 \left[1 + b_2 P_2(\cos\theta) + b_4 P_4(\cos\theta)\right] \tag{5}$$

has been fitted to the data points. A comparison of the experimental and theoretical angular distributions for series A is presented in Fig. 7 and the fitted coefficients of Eq. (5) are listed in Table III. The theoretical angular distribution appears to be flatter than the experimental one in the range from 90° to 130°, while the point at 150° is well-reproduced. Such shape of the angular distribution is a direct consequence of the previously described discrepancies in the shapes of the reconstructed theoretical lines. Series B has been neglected in this comparison, since the number of experimental points is not sufficient to conduct a fit using Eq. (5).

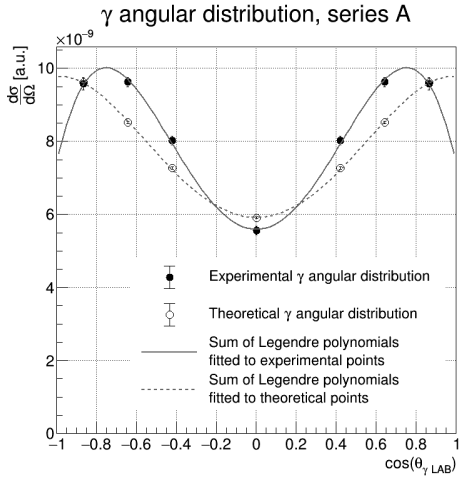


Fig. 7. A comparison of the experimental gamma angular distribution (bullets) and the angular distribution based on the model of the $^{12}\mathrm{C}_{4.44\to\mathrm{gs}}$ line (circles). A sum of Legendre polynomials has been fitted to the experimental data points (solid line) and theoretical points (dotted line).

TABLE III

Fitted coefficients of equation (5) for series A.

| | Experimental points | Theoretical points |
|---|---|---|
| $b_0$ | $8.044(50) \times 10^{-9}$ | $7.771(12) \times 10^{-9}$ |
| $b_2$ | 0.316(17) | 0.3818(41) |
| $b_4$ | −0.391(23) | −0.1259(55) |

In order to investigate the effect of energy loss by excited carbon nucleus on the results of the model, we repeated the calculations without this effect. Obtained fitting results are listed in Table IV. Values of parameters $a_0$ and $a_2$ differ significantly from those presented in Table II. The corresponding $\chi^2$ distributions maps are shown in Fig. 8 and can be compared to those in Fig. 6. It can be observed that minima are shifted along the hypotenuse of the physical area triangle. At the same time, the sizes and shapes of minima remain comparable. This proves large influence of the carbon nucleus deceleration in the investigated nuclear process and shape of the associated spectral line.

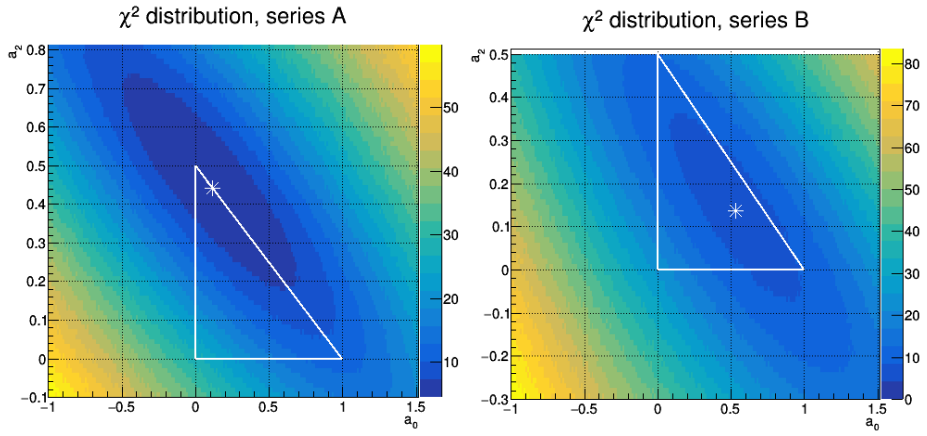


Fig. 8. (Color online) $\chi^2$ distribution maps calculated assuming constant velocity of excited carbon. The asterisk indicates values of the parameters $a_0$ and $a_2$ determined by the fitting procedure. The triangle indicates the area where parameters have physically valid values.

TABLE IV

Values of parameters describing the shape of the $^{12}C_{4.44\to gs}$ line for model implementation with constant velocity of excited carbon nucleus.

| Parameter | Series A | Series B |
|---|---|---|
| $a_0$ | 0.166(48) | 0.529(15) |
| $a_2$ | 0.442(35) | 0.137(20) |
| $h$ | $2.03(29) \times 10^{-7}$ | $2.98(34) \times 10^{-7}$ |

The difference between the values of $a_0$ and $a_2$ parameters as well as the shift of the $\chi^2$ distribution minimum is larger for series B. This can be explained by different mean energy of protons interacting with target carbon nuclei. For series B, mean proton energy is smaller (see Fig. 3), thus also recoil energy is smaller and energy loss, *i.e.* deceleration of excited carbon nucleus, is larger.

## 5. Conclusions

The model describing the shape of the spectral line from the $^{12}C(p,p'\gamma_{4.44})^{12}C$ nuclear reaction has been used for description of the experimental data. The implementation of the model uses a Monte-Carlo-based calculation techniques and it assumes that the investigated nuclear reaction occurs in two stages. The results of calculations have been subsequently compared with the experimental data in order to find the values of parameters providing the best match to the shape of the $^{12}C_{4.44\to gs}$ spectral line and, therefore, also the gamma angular distribution of the reaction. In this study, two experimental series consisting of measurements for different proton energies and detection angles have been analyzed.

The model calculations delivered gamma energy spectra for different angles and angular distribution of the nuclear reaction. These results are consistent with the experimental data. Minor discrepancies between them are probably caused by approximations in the input data set. Additional tests proved that the model calculations give consistent results.

Additionally, the importance of the energy loss of the excited carbon nucleus in the target was investigated. A comparison between two implementations, one of which assumed the carbon nucleus moving at a constant velocity and the other one, in which it slowed down, showed significant differences in obtained results. This proves that the effect cannot be neglected in the calculations as it has large influence on the shape of the $^{12}C_{4.44\to gs}$ line and parameters of the gamma emission angular distribution.

We wish to acknowledge the staff of the Heidelberg Ion-Beam Therapy Center for a good atmosphere and their support of the technical aspects of the experiment. We also thank Edward Stephenson for careful revision of the manuscript. The research is part of the project *Investigation of gamma emission in experimental modeling of hadron therapy* carried out within the POMOST programme of the Foundation for Polish Science, cofinanced from the European Union under the European Regional Development Found.

## REFERENCES

[1] J.J. Kolata, R. Auble, A. Galonsky, *Phys. Rev.* **162**, 957 (1967).
[2] P. Dyer *et al.*, *Phys. Rev. C* **23**, 1865 (1981).
[3] B. Kozlovsky, R. Ramaty, R.E. Lingenfelter, *Astrophys. J.* **484**, 286 (1997).
[4] R.J. Murphy, B. Kozlovsky, R. Ramaty, *Astrophys. J.* **331**, 1029 (1988).
[5] J. Kiener, N. de Séréville, V. Tatischeff, *Phys. Rev. C* **64**, 025803 (2001).
[6] J.M. Blatt, V.F. Weisskopf, *Theoretical Nuclear Physics*, Springer-Verlag, 1979, p. 594.
[7] K. Rusiecka *et al.*, *World J. Nucl. Sci. Technol.* **6**, 63 (2016).
[8] L. Kelleter *et al.*, *Phys. Med.* **34**, 7 (2017).
[9] R. Brun, F. Rademakers, ROOT a Data Analysis Framework (computer software), https://root.cern.ch/, Version 5.34/25, 2015.
[10] Geant4 (computer software), http://geant4.web.cern.ch/geant4/index.shtml, Version 9.6.1, 2015.
[11] M. Duijvestijn, A. Koning, S. Hilaire, Talys (computer software), http://www.talys.eu/home/, Version 1.8, 2006.
[12] M. Tomita *et al.*, *Phys. Rev. C* **95**, 024609 (2015).
[13] J.K. Dickens, D.A. Haner, C.N. Waddell, *Phys. Rev.* **129**, 743 (1963).
[14] J.K. Dickens, D.A. Haner, C.N. Waddell, *Phys. Rev.* **132**, 2158 (1963).
[15] L.N. Blumberg *et al.*, *Phys. Rev.* **147**, 812 (1966).
[16] S. Kato *et al.*, *Phys. Rev. C* **31**, 1616 (1985).
[17] K. Hosono *et al.*, *Phys. Rev. Lett.* **41**, 621 (1978).
[18] E.L. Petersen *et al.*, *Nucl. Phys. A* **102**, 145 (1967).
[19] J.A. Fannon, E.J. Burge, D.A. Smith, N.K. Ganguly, *Nucl. Phys. A* **97**, 263 (1967).
[20] W.E. Burcham, W.M. Gibson, A. Hossain, J. Rotblat, *Phys. Rev.* **92**, 1266 (1953).
[21] G.E. Fisher, *Phys. Rev.* **96**, 704 (1954).
[22] R.W. Peelle, *Phys. Rev.* **105**, 1311 (1957).
[23] H.E. Conzett, *Phys. Rev.* **105**, 1324 (1957).
[24] Nuclear Levels and Gamma Search, http://www.nndc.bnl.gov/nudat2/indx_adopted.jsp, accessed: 2018-05-22.
[25] J. Ziegler, SRIM (computer software), http://www.srim.org/, 2013.